11636 *Inorg. Chem.* **2009**, *48*, 11636–11645
DOI: 10.1021/ic901641f

Inorganic Chemistry
Article

Wheel-Shaped Cu_{20}-Tungstophosphate $[Cu_{20}X(OH)_{24}(H_2O)_{12}(P_8W_{48}O_{184})]^{25-}$ Ion (X = Cl, Br, I) and the Role of the Halide Guest

Sib Sankar Mal,[†] Bassem S. Bassil,[†] Masooma Ibrahim,[†] Saritha Nellutla,[‡] Johan van Tol,[‡,§] Naresh S. Dalal,[‡,§] Jorge A. Fernández,[∥] Xavier López,[∥] Josep M. Poblet,[∥] Rosa Ngo Biboum,[⊥] Bineta Keita,[⊥] and Ulrich Kortz*[,†]

[†]*School of Engineering and Science, Jacobs University, P.O. Box 750 561, 28725 Bremen, Germany,* [‡]*Department of Chemistry and Biochemistry, Florida State University, Tallahassee, Florida 32306,* [§]*Center for Interdisciplinary Magnetic Resonance, National High Magnetic Field Laboratory, Tallahassee, Florida 32310,* [∥]*Departament de Química Física i Inorgànica, Universitat Rovira i Virgili, Imperial Tàrraco 1, 43005 Tarragona, Spain, and* [⊥]*Laboratoire de Chimie Physique, Groupe d'Electrochimie et de Photoélectrochimie, UMR 8000, CNRS, Université Paris-Sud, Bâtiment 350, 91405 Orsay cedex, France*

Received August 16, 2009

We have synthesized the known $[Cu_{20}Cl(OH)_{24}(H_2O)_{12}(P_8W_{48}O_{184})]^{25-}$ (**1**) and report here its bromide and iodide analogues, $[Cu_{20}Br(OH)_{24}(H_2O)_{12}(P_8W_{48}O_{184})]^{25-}$ (**2**) and $[Cu_{20}I(OH)_{24}(H_2O)_{12}(P_8W_{48}O_{184})]^{25-}$ (**3**). These polyanions were characterized in the solid state by IR spectroscopy and single-crystal X-ray diffraction. Magnetic susceptibility and magnetization data over 1.8−300 K show that the Cu^{2+} ions in **1**−**2** are antiferromagnetically coupled, leading to a diamagnetic ground state. The effective exchange coupling constant J_{eff} was estimated as ~ -3 K for both **1** and **2**. Electron paramagnetic resonance measurements were made on **1** and **2** over 5−295 K at microwave frequencies of 9.5, 34, and 220 GHz. The observed (weak) signals were characteristic of randomly distributed Cu^{2+} ions only, with g values and hyperfine constants typical of the unpaired electron in a $3d_{x^2-y^2}$ orbital of Cu^{2+}. No signals attributable to the copper-hydroxo cluster were detected, supporting the conclusions from the magnetization measurements. DFT calculations were performed as well to obtain additional information on the anionic guest inside the cavity created by the copper-hydroxo cage related to electronic structure and energies of encapsulation. The polyanions **2** and **3** were also characterized by cyclic voltammetry (CV) in a pH 5 medium. Their CVs are composed by an initial two-step reduction of the Cu^{2+} centers to Cu^0 through Cu^+, followed at more negative potential by the redox processes of the W centers. A comparison with the CV characteristics of the previously studied compound **1** indicates that the potential locations of the Cu or W waves of the three analogues do not depend significantly upon the identity of the central halide X. This observation is in accordance with conclusions of DFT calculations. The modified electrodes based on **2** and the room-temperature ionic liquid 1-butyl-3-methylimidazolium tetrafluoroborate triggers an efficient reduction of nitrate. To our knowledge, this is the first example of electrocatalytic nitrate reduction by a polyanion entrapped in room-temperature ionic liquid films.

Introduction

Polyoxometalates (POMs) represent a unique class of anionic metal−oxygen clusters with large structural versatility and a range of chemical and physical properties.[1] Of special interest are lacunary-type POMs, which can act as inorganic ligands by coordinating to different types of electrophiles, especially transition metal centers. In particular, Keggin and Dawson type heteropolytungstates are of interest in this respect.[1a] Lacunary POMs are derived from plenary parent structures by loss of one or more addenda atoms. Incorporation of magnetic ions in these vacant sites usually preserves the POM structure but, in some cases, can also lead to isomerization or even loss or gain of tungsten. In any case, the resulting products are usually good candidates for magnetic, electrochemical, and catalytic studies.[2]

*To whom correspondence should be addressed. Fax: +49-(0)421-200-3229. E-mail: u.kortz@jacobs-university.de.

(1) (a) Pope, M. T. *Heteropoly and Isopoly Oxometalates*; Springer-Verlag: Berlin, 1983. (b) Pope, M. T.; Müller, A. *Angew. Chem., Int. Ed. Engl.* **1991**, *30*, 34. (c) Pope, M. T. *Comp. Coord. Chem. II* **2003**, *4*, 635. (d) Hill, C. L. *Comp. Coord. Chem. II* **2003**, *4*, 679. (e) *Polyoxometalate Molecular Science*; Borràs-Almenar, J. J., Coronado, E., Müller, A., Pope, M. T., Eds.; Kluwer: Dordrecht, The Netherlands, 2004.

(2) (a) *Polyoxometalates: From Platonic Solids to Anti-Retroviral Activity*; Pope, M. T., Müller, A., Eds.; Kluwer: Dordrecht, The Netherlands, 1994. (b) Müller, A.; Reuter, H.; Dillinger, S. *Angew. Chem., Int. Ed. Engl.* **1995**, *34*, 2328. (c) Hill, C. *Chem. Rev.* **1998** (special thematic issue on polyoxometalates). (d) *Polyoxometalate Chemistry: From Topology via Self-Assembly to Applications*; Pope, M. T.; Müller, A., Eds.; Kluwer: Dordrecht, The Netherlands, 2001. (e) *Polyoxometalate Chemistry for Nano-Composite Design*; Yamase, T., Pope, M. T., Eds.; Kluwer: Dordrecht, The Netherlands, 2002.

 Published on Web 11/25/2009

Tungstophosphates comprise the largest class of plenary and lacunary heteropoly precursors, and most of them are derived from the Keggin and Wells-Dawson structures. Most common examples are the trilacunary Keggin ion $[PW_9O_{34}]^{9-}$, the trilacunary Wells-Dawson ion $[P_2W_{15}O_{56}]^{12-}$, or the hexalacunary Wells-Dawson ion $[H_2P_2W_{12}O_{48}]^{12-}$.[1a] The latter can in turn be used as a precursor for the formation of the crown-shaped superlacunary ion $[H_7P_8W_{48}O_{184}]^{33-}$ $\{P_8W_{48}\}$, which comprises four $\{P_2W_{12}\}$ units connected to each other via the caps. Unlike $[H_2P_2W_{12}O_{48}]^{12-}$, which is rather unstable and highly reactive in solution, $\{P_8W_{48}\}$ is very stable in aqueous solution over an unusually large pH range (1−8). The cavity of the cyclic precursor is expected to be nucleophilic, as indicated by the presence of numerous potassium ions in the potassium salt of $\{P_8W_{48}\}$. In 1985, Contant and Tézé reported that $\{P_8W_{48}\}$ "does not give complexes with divalent or trivalent transition metal ions".[3] Twenty years later, our group was able to incorporate a 20-copper-hydroxo cluster in the cavity of $\{P_8W_{48}\}$ resulting in $[Cu_{20}Cl(OH)_{24}(H_2O)_{12}(P_8W_{48}O_{184})]^{25-}$ (**1**), by a simple one-pot reaction of the cyclic polyanion precursor with Cu^{2+} ions in an aqueous lithium acetate buffer.[4] This Cu_{20}-hydroxo cluster exhibits three types of copper centers with respect to their coordination environment (octahedral, square-pyramidal, and square-planar). We have already described the solid-state and solution properties of **1** in detail, as well as studies in the areas of electrochemistry, surface science, vesicle formation, and oxidation catalysis.[5]

An azide-bridged derivative of **1**, $[P_8W_{48}O_{184}Cu_{20}(N_3)_6(OH)_{18}]^{24-}$, has also been reported by Mialane and co-workers.[6] Other derivatives of the crown-shaped $\{P_8W_{48}\}$ include Pope's lanthanide species $\{Ln_4(H_2O)_{28}[K\subset P_8W_{48}O_{184}(H_4W_4O_{12})_2Ln_2(H_2O)_{10}]^{13-}\}_x$ (Ln = La, Ce, Pr, Nd), Müller's/Pope's mixed-valence vanadium species $[K_8\{P_8W_{48}O_{184}\}\{V^V_4V^{IV}_2O_{12}(H_2O)_2\}_2]^{24-}$, and Cronin's cobalt-derivatives.[7] Our group also synthesized an organo-ruthenium derivative, $\{K(H_2O)\}_3\{Ru(p\text{-cymene})(H_2O)\}_4P_8W_{49}O_{186}(H_2O)_2]^{27-}$, and the Fe_{16}-containing $[P_8W_{48}O_{184}Fe_{16}(OH)_{28}(H_2O)_4]^{20-}$ (which was also identified independently by Müller and co-workers).[8]

Here, we describe the synthesis and structure of derivatives of **1** with the central chloride guest replaced by bromide and iodide. Furthermore, we report on electrochemical, magnetic/electron paramagnetic resonance (EPR), and density functional theory (DFT) studies.

Experimental Section

Synthesis. We used reagent-grade chemicals as-purchased without further purification. $K_{28}Li_5[H_7P_8W_{48}O_{184}]\cdot 92H_2O$ was prepared according to the published procedure and then washed with 2 M KNO_3 in order to remove any remaining chloride ions resulting from the synthesis procedure of the POM precursor.[3]

Synthesis of $K_{12}Li_{13}[Cu_{20}Cl(OH)_{24}(H_2O)_{12}(P_8W_{48}O_{184})]\cdot 22H_2O$ (KLi-1). The synthesis of **KLi-1** was performed according to our previously reported procedure.[4]

Synthesis of $K_{12}Li_{13}[Cu_{20}Br(OH)_{24}(H_2O)_{12}(P_8W_{48}O_{184})]\cdot 60H_2O$ (KLi-2). A sample of $CuBr_2\cdot 2H_2O$ (0.17 g, 0.66 mmol) was dissolved in a 1 M $LiCH_3COO$ buffer solution (20 mL) at pH 6.0; then, $K_{28}Li_5[H_7P_8W_{48}O_{184}]\cdot 92H_2O$ (0.37 g, 0.025 mmol) was added. This solution was heated at 80 °C for 1 h and filtered while hot. The filtrate was allowed to evaporate in an open beaker at room temperature. After about a day, a blue crystalline product started to appear. Evaporation was allowed to continue until the solution level had approached the solid product, which was then collected by filtration and air-dried. Yield: 0.18 g (46%). IR: 1120, 1080, 1017, 951, 936, 904, 842, 752, 681, 523, 470 cm^{-1}. Elem anal. calcd (found): K, 3.0 (3.1),; Li, 0.6 (0.5); Cu, 8.1 (7.4); W, 56.5 (57.9); P, 1.6 (1.6); Br, 0.51 (0.47).

Synthesis of $K_{12}Li_{13}[Cu_{20}I(OH)_{24}(H_2O)_{12}(P_8W_{48}O_{184})]\cdot 50H_2O$ (KLi-3). A sample of $CuSO_4\cdot 5H_2O$ (0.17 g, 0.66 mmol) was dissolved in a 1 M $LiCH_3COO$ buffer solution (20 mL) at pH 6.0; then, $K_{28}Li_5[H_7P_8W_{48}O_{184}]\cdot 92H_2O$ (0.37 g, 0.025 mmol) was added followed by the addition of NaI (0.036 g, 0.24 mmol). The solution was heated at 80 °C for 1 h and then filtered while hot. The filtrate was allowed to evaporate in an open vial at room temperature. After about 5−6 days, a blue crystalline product started to appear. Evaporation was allowed to continue until the solution level had reached the solid product, which was then collected by filtration and air-dried. Yield: 0.044 g (11%). IR: 1120, 1078, 1016, 948, 934, 904, 830, 752, 685, 527, 470 cm^{-1}. Elem anal. calcd (found): K, 3.0 (2.7); Li, 0.6 (0.4); Cu, 8.2 (7.9); W, 56.9 (57.0); P, 1.6 (1.6); I, 0.82 (0.86).

Instrumentation. Infrared spectra were recorded on KBr pellets using a Nicolet Avatar 370 spectrometer. Elemental analyses for K, Li, Cu, W, and P were carried out by Gesellschaft für Laboruntersuchungen mbH, Wesseling, Germany, and analyses for Br and I were performed by Analytische Laboratorien, Lindlar, Germany. All NMR spectra were recorded on a 400 MHz JEOL ECX instrument at room temperature using H_2O/D_2O as the solvent.

X-Ray Crystallography. Crystals were mounted in Hampton cryoloops using light oil for data collection at 173 K. Indexing and data collection were performed using a Bruker X8 APEX II CCD diffractometer with κ geometry and Mo Kα radiation (λ = 0.71073 Å). Data integration and routine processing were performed using the SAINT software suite. Further data processing, including multiscan absorption corrections, was performed using SADABS.[9] Direct method (SHELXS97) solutions successfully located the W atoms, and successive Fourier syntheses (SHELXL97) revealed the remaining atoms.[10] Refinements were full-matrix least-squares against F^2 using all data. All nondisordered heavy atoms (P, Cu, W, K, Br, I) were refined anisotropically, while the O atoms and a few disordered K countercations were refined with fractional occupancies. No H or Li atoms were included in the models. The crystallographic data are summarized in Table 1.

(3) (a) Contant, R.; Tézé, A. *Inorg. Chem.* **1985**, *24*, 4610. (b) Contant, R. *Inorg. Synth.* **1990**, *27*, 110.

(4) Mal, S. S.; Kortz, U. *Angew. Chem., Int. Ed.* **2005**, *44*, 3777.

(5) (a) Jabbour, D.; Keita, B.; Nadjo, L.; Kortz, U.; Mal, S. S. *Electrochem. Commun.* **2005**, *7*, 841. (b) Alam, M. S.; Dremov, V.; Müller, P.; Postnikov, A. V.; Mal, S. S.; Hussain, F.; Kortz, U. *Inorg. Chem.* **2006**, *45*, 2866. (c) Liu, G.; Liu, T.; Mal, S. S.; Kortz, U. *J. Am. Chem. Soc.* **2006**, *128*, 10103. (d) Liu, G.; Liu, T.; Mal, S. S.; Kortz, U. *J. Am. Chem. Soc.* **2007**, *129*, 2408. (e) Chen, L.; Hu, J.; Mal, S. S.; Kortz, U.; Jaensch, H.; Mathys, G.; Richards, R. M. *Chem.—Eur. J.* **2009**, *15*, 7490.

(6) Pichon, C.; Mialane, P.; Dolbecq, A.; Marrot, J.; Rivière, E.; Keita, B.; Nadjo, L.; Sécheresse, F. *Inorg. Chem.* **2007**, *46*, 5292.

(7) (a) Zimmermann, M.; Belai, N.; Butcher, R. J.; Pope, M. T.; Chubarova, E. V.; Dickman, M. H.; Kortz, U. *Inorg. Chem.* **2007**, *46*, 1737. (b) Müller, A.; Pope, M. T.; Todea, A. M.; Bögge, H.; van Slageren, J.; Dressel, M.; Gouzerh, P.; Thouvenot, R.; Tsukerblat, B.; Bell, A. *Angew. Chem., Int. Ed.* **2007**, *46*, 4477. (c) Mitchell, S. G.; Gabb, D.; Ritchie, C.; Hazel, N.; Long, D.-L.; Cronin, L. *CrystEngComm* **2009**, *11*, 36.

(8) (a) Mal, S. S.; Nsouli, N. H.; Dickman, M. H.; Kortz, U. *Dalton Trans.* **2007**, 2627. (b) Mal, S. S.; Dickman, M. H.; Kortz, U.; Todea, A. M.; Merca, A.; Bögge, H.; Glaser, T.; Müller, A.; Nellutla, S.; Kaur, N.; van Tol, J.; Dalal, N. S.; Keita, B.; Nadjo, L. *Chem.—Eur. J.* **2008**, *14*, 1186.

(9) Sheldrick, G. M. *SADABS*; University of Göttingen: Göttingen, Germany, 1996.

(10) Sheldrick, G. M. *SHELXS-97*; University of Göttingen: Göttingen, Germany, 1997.

Table 1. Crystal Data and Structure Refinement for **KLi-2** and **KLi-3**

empirical formula	$K_{12}Li_{13}[Cu_{20}Br(OH)_{24}(H_2O)_{12}(P_8W_{48}O_{184})]\cdot 60H_2O$ (**KLi-2**)	$K_{12}Li_{13}[Cu_{20}I(OH)_{24}(H_2O)_{12}(P_8W_{48}O_{184})]\cdot 50H_2O$ (**KLi-3**)
mw	16235.5	15498.4
cryst syst	tetragonal	tetragonal
space group (no.)	*P*4/*m* (83)	*I*4/*m* (87)
a/Å	24.0953(2)	26.9335(3)
b/Å	24.0953(2)	26.9335(3)
c/Å	21.9359(5)	21.0993(7)
V/Å^3	12735.6(3)	15305.7(6)
Z	2	2
T/°C	−100	−100
λ/Å	0.71073	0.71073
D_{calcd}/Mg m^{-3}	4.091	3.442
μ/mm^{-1}	23.061	20.260
R [I < 2*σ*(I)][a]	0.0457	0.0700
R_w (all data)[b]	0.1427	0.2179

[a] $R = \sum||F_o| - |F_c||/\sum|F_o|$. [b] $R_w = [\sum w(F_o^2 - F_c^2)^2/\sum w(F_o^2)^2]^{1/2}$.

Magnetic Susceptibility and Magnetization Measurements. A Quantum Design MPMS SQUID magnetometer was used to collect the magnetic susceptibility data on powder samples of **KLi-1** and **KLi-2** in the temperature range of 1.8−300 K with an applied magnetic field of 0.1 tesla (T) and magnetization data at 1.8 K from 0 to 7 T. The diamagnetic and temperature-independent paramagnetism correction terms have been combined into one constant in the susceptibility data analysis and were obtained as $\sim -2 \times 10^{-4}$ and $\sim 8 \times 10^{-4}$ emu/mol for **KLi-1** and **KLi-2**, respectively.

EPR Measurements. Polycrystalline powder EPR spectra of **KLi-1** and **KLi-2** were recorded at ~9.5 to 220 GHz. The 9.5 and 34 GHz spectra were obtained using a commercial Bruker Elexys 680 spectrometer, whereas the high-frequency data were collected on home-built instruments at the National High Magnetic Field Laboratory in Tallahassee, Florida.[11] The temperature was varied from ambient temperature to 5 K. The modulation amplitude and microwave power were adjusted for optimal signal intensity and resolution.

Computational Details. Calculations were carried out with the DFT formalism using the ADF2007.01 package.[12] We applied the local density approximation featuring the Xα model with Becke's functional for exchange and the VWN parametrization with Perdew's correction for correlation.[13−15] Geometry optimizations were carried out with a Slater basis of the DZ quality for describing the valence electrons of all of the atoms, except for chlorine and the oxygens of the Cu_{20} framework, for which we used the TZP basis set. The internal or core electrons (C, N, O 1s; P, Cu, Cl 1s-2p; Cl 1s−2p; Br 1s−3p; I 1s−4p; W 1s−4f) were frozen and described by single Slater functions. We applied scalar relativistic corrections to the internal electrons by means of the zeroth-order regular approximation, via the core potentials generated with the program DIRAC.[12] Geometry optimizations were performed leaving the $\{P_8W_{48}\}$ fragment frozen at the experimental geometry and fully optimizing the Cu_{20} moiety. Then, single-point calculations at the optimized geometry were performed using a Slater TZP basis set and the COSMO method to introduce the solvent effects of water.[16] The formalism utilized for the open-shell electronic configurations is the unrestricted SCF. The system is thus described by 2492 valence electrons through 3601 basis functions in the gas-phase calculations and 6405 basis functions in single-point solvent calculations. DFT calculations were driven for the entire molecule of 345 atoms, 68 of which are metals.

Electrochemistry. a. Materials, Apparatus, Procedures. The solutions were deaerated thoroughly for at least 30 min with pure argon and kept under a positive pressure of this gas during the experiments. The source, mounting, and polishing of the glassy carbon (GC, Tokai, Japan) electrodes have been described elsewhere.[17] The glassy carbon samples had a diameter of 3 mm. Controlled potential coulometry was carried out with a large surface area glassy carbon plate. The electrochemical setup was an EG&G 273 A driven by a PC with the M270 software. Potentials are quoted against a saturated calomel electrode (SCE). The counterelectrode was a platinum gauze of large surface area. All experiments were performed at room temperature.

The UV−visible spectra were recorded with a Lambda 19 Perkin-Elmer spectrophotometer. All solutions were 7.3×10^{-6} M in POM and were placed in quartz cuvettes with an optical path of 1 cm. The composition of the aqueous medium was 1 M $CH_3COOLi + CH_3COOH$ (pH 5). The room-temperature ionic liquid was 1-butyl-3-methylimidazolium tetrafluoroborate (**$BMImBF_4$**). All chemicals were of high-purity grade and were used as-purchased without further purification.

b. Preparation of Modified Electrodes. The electrode material was either a polished GC[17] or an ITO plate. Prior to the modification processes, the ITO plate was pretreated according to the literature method.[18] It was sonicated in acetone for 10 min, rinsed with water, treated by ultrasonic agitation in concentrated NaOH in 1:1 (v/v) water ethanol for 10 min, rinsed with water, and finally dried with nitrogen. A modified literature method was used[19] for the immobilization of the POMs@ **$BMImBF_4$** film on the working electrode substrate. Typically, a sample of GC or ITO was immersed in a **$BMImBF_4$** solution of **2** (0.4 mM) for 1 min. The film-coated electrode was then maintained at 80 °C for 2 h.

c. Stability Studies of 2 and 3. Before studying the redox properties of **2** and **3**, it was necessary to determine their stability domain over the pH scale being used. In fact, it is known that POMs may undergo chemical transformations or completely decompose depending on pH, the composition of the solution in which they are dissolved, and POM concentration. The classical media used for electrochemical studies are, in general, different from those utilized for other characterization techniques such as NMR. Furthermore, POM concentrations used for electrochemical characterisations are relatively low. UV−visible spectroscopy proved very useful for investigating POM stability under such conditions. POM stability could also be confirmed by cyclic voltammetry.

The stability tests of the oxidized forms of **2** and **3** as a function of time were studied at pH 5 (1 M $CH_3COOLi + CH_3COOH$) by monitoring their UV−visible spectrum. The spectra were recorded over a period of at least 24 h. This duration was selected as a compromise between the time needed

(11) (a) Cage, B.; Hassan, A. K.; Pardi, L.; Krzystek, J.; Brunel, L. C.; Dalal, N. S. *J. Magn. Reson.* **1997**, *124*, 495. (b) Hassan, A. K.; Pardi, L. A.; Krzystek, J.; Sienkiewicz, A.; Goy, P.; Rohrer, M.; Brunel, L. C. *J. Magn. Reson.* **2000**, *142*, 300.

(12) (a) *ADF 2007.01*; Department of Theoretical Chemistry, Vrije Universiteit: Amsterdam, 2007. (b) Baerends, E. J.; Ellis, D. E.; Ros, P. *Chem. Phys.* **1973**, *2*, 41. (c) Versluis, L.; Ziegler, T. *J. Chem. Phys.* **1988**, *88*, 322. (d) Te Velde, G.; Baerends, E. J. *J. Comput. Phys.* **1992**, *99*, 84. (e) Fonseca Guerra, C.; Snijders, J. G.; Te Velde, G.; Baerends, E. J. *Theor. Chem. Acc.* **1998**, *99*, 391. (f) Te Velde, G.; Bickelhaupt, F. M.; van Gisbergen, S. J. A.; Fonseca Guerra, C.; Baerends, E. J.; Snijders, J. G.; Ziegler, T. *J. Comput. Chem.* **2001**, *22*, 931.

(13) (a) Becke, A. D. *J. Chem. Phys.* **1986**, *84*, 4524. (b) Becke, A. D. *Phys. Rev.* **1988**, *A38*, 3098.

(14) Vosko, S. H.; Wilk, L.; Nusair, M. *Can. J. Phys.* **1980**, *58*, 1200.

(15) (a) Perdew, J. P. *Phys. Rev.* **1986**, *B33*, 8822. (b) Perdew, J. P. *Phys. Rev.* **1986**, *B34*, 7406.

(16) (a) Klamt, A.; Schürmann, G. *J. Chem. Soc, Perkin Trans. 2* **1993**, 799. (b) Andzelm, J.; Kölmel, C.; Klamt, A. *J. Chem. Phys.* **1995**, *103*, 9312. (c) Klamt, A. *J. Chem. Phys.* **1995**, *99*, 2224. (d) Model implemented in the ADF package by: Pye, C. C.; Ziegler, T. *Theor. Chem. Acc.* **1999**, *101*, 396.

(17) Keita, B.; Nadjo, L. *J. Electroanal. Chem.* **1988**, *243*, 87.

(18) Shan, Y.; Yang, G.; Sun, Y.; Pang, S.; Gong, J.; Su, Z.; Qu, L. *Electrochim. Acta* **2007**, *53*, 569.

(19) Huang, B.-Q.; Wang, L.; Shi, K.; Xie, Z.-X.; Zheng, L.-S. *J. Electroanal. Chem.* **2008**, *615*, 19.

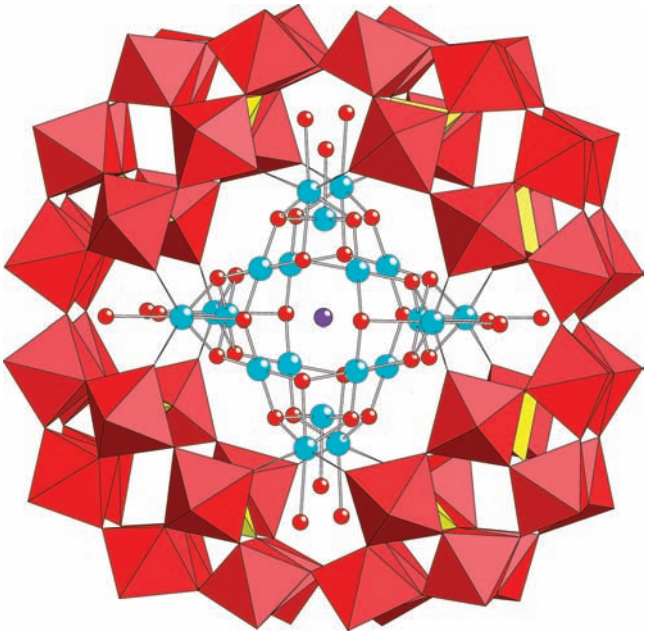

Figure 1. Combined ball-and-stick/polyhedral representation of polyanions **1**−**3**. The color code is as follows: WO_6, red; PO_4, yellow; Cu, turquoise; O, red; and halide X, blue.

for electrochemical characterization of the polyanions and that for eventual long-lasting or preparative catalytic or electrocatalytic processes. The spectra of **2** and **3** were characterized by a main peak located between 248 and 278 nm. They were reproducible with respect to absorbances and wavelengths for at least 24 h. This observation is in agreement with the previous one made with **1**,[5a] under the same experimental conditions.

Result and Discussion

Synthesis and Structure. The synthesis of polyanions **2** and **3** follows the same strategy as for polyanion **1** except that different copper(II) salts were used. As a bromide source, $CuBr_2$ was used instead of $CuCl_2$, and for the iodide derivative, $CuSO_4$ was used with NaI as the halide source. Both **2** and **3** crystallize as mixed lithium potassium salts in two different tetragonal space groups: $P4/m$ for **KLi-2** and $I4/m$ for **KLi-3**, see Table 1. Polyanions **1**−**3** are isostructural, see Figure 1. They comprise a $\{Cu_{20}(OH)_{24}(H_2O)_{12}\}^{16+}$ cluster imbedded inside the $\{P_8W_{48}\}$ ring, resulting in an assembly with D_{4h} symmetry. The main difference between the three analogues lies in the halogen guest X trapped inside the copper-hydroxo cluster. The shortest Cu−X distances in **1** (3.362(3)), **2** (3.369(2)), and **3** (3.383(3)), involving the eight Cu^{2+} ions with square-planar coordination, are very similar, indicating that the three different halides Cl^-, Br^- and I^- do not affect the dimensions of the Cu_{20}-hydroxo cluster significantly. The ^{31}P NMR chemical shifts for solutions of **1** (−29.3 ppm), **2** (−29.1 ppm), and **3** (−29.3 ppm) are very similar, indicating that halide substitution has no significant effect, see Figures S1 and S2 (Supporting Information).

Magnetic Susceptibility and Magnetization. Detailed magnetic susceptibility, magnetization, and variable-frequency EPR measurements were undertaken on **KLi-1** and **KLi-2** with the view of detecting any magnetic ordering or spin glass behavior of the Cu_{20} clusters. The magnetic behaviors of **KLi-1** and **KLi-2** were found to be

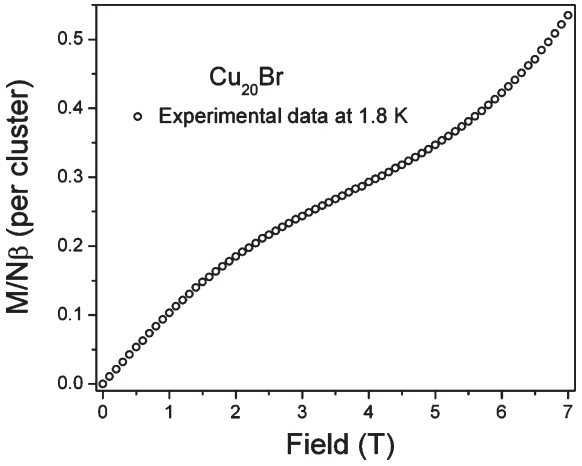

Figure 2. Observed magnetization (BM per polyanion) of **KLi-2** plotted as reduced magnetization ($M/N\beta$) versus magnetic field.

similar, and neither one exhibited any magnetic transition over the range of 1.8−300 K. As an example, Figure 2 shows the data for **KLi-2**, where we have plotted the magnetic moment per mole of the cluster, $M/N\beta$ versus magnetic field in tesla. The measured saturation magnetic moment of 0.55 μ_B (Bohr magneton) at 7 T is much less than the expected value of 1.075 μ_B (one electron with $g = 2.15$), suggesting that antiferromagnetic interactions are dominant in **2**, resulting in a diamagnetic spin singlet ground state.[20] The inflection around 3.5 T is probably due to the crossing of some of the excited states with the ground state, leading to an enhanced magnetization. A similar behavior was observed for **1**.

Figure 3 displays the magnetic susceptibility of **KLi-2** as χ versus T and χT versus T. The χ versus T profile clearly indicates that *all* of the Cu^{2+} ions in the Cu_{20} cluster are strongly antiferromagnetically coupled, leading to a near cancellation of the magnetic moment in the ground state. A rapid increase in the susceptibility below ~3.5 K is attributed to traces of randomly distributed countercationic Cu^{2+} ions, which create a Curie tail and a large increase in the magnetic susceptibility. This is consistent with our detailed EPR studies (vide infra).

On the basis of the structures of **1** and **2**, we require at least three exchange coupling constants (J_1, J_2, and J_3) to describe the $Cu^{2+}\cdots Cu^{2+}$ spin exchange interactions in Cu_{20}. A review of the bond angles, ranging from 90−120°, and bond distances, ranging from 2.8−3.3 Å, suggests that both ferro- and antiferromagnetic interactions are present, and their magnitudes are probably very close to each other. This situation might result in a small effective exchange coupling constant (J_{eff}), which in turn can lead to very closely spaced spin energy levels. Because of the large Hilbert space ($2^{20} \times 2^{20}$), the assumption $J_1 = J_2 = J_3 = J_{eff}$ has been evoked to analyze the magnetic susceptibility data. Furthermore, only high-temperature data (25−300 K) will be considered to better include the paramagnetic excited spin states and to avoid the contributions from the randomly distributed paramagnetic Cu^{2+} countercation impurity. The spin exchange Hamiltonian shown in eq 1 is used

(20) Expected value is calculated from $M_{sat} = N\beta gS$.

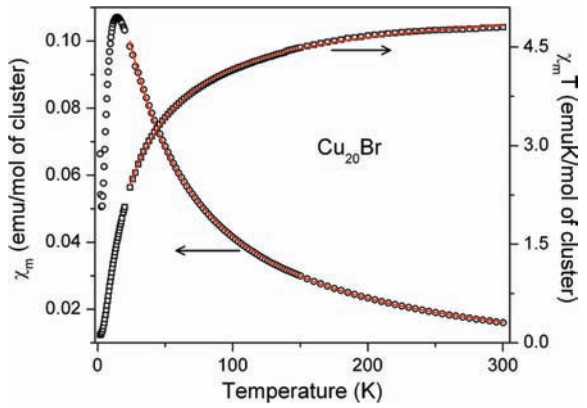

Figure 3. Observed magnetic susceptibility of **KLi-2** plotted as electromagnetic unit per mole of polyanion. The increase in χ below ~3.5 K is attributed to a Cu^{2+} countercation impurity. The solid line is a fit of the experimental data to the Hamiltonian in eq 1. See the text for more details.

to estimate J_{eff}.

$$\begin{aligned}\hat{H} = -2J_{eff}[&\hat{S}_1\cdot\hat{S}_2+\hat{S}_2\cdot\hat{S}_3+\hat{S}_3\cdot\hat{S}_4+\hat{S}_4\cdot\hat{S}_5\\&+\hat{S}_5\cdot\hat{S}_6+\hat{S}_6\cdot\hat{S}_7+\hat{S}_7\cdot\hat{S}_8+\hat{S}_8\cdot\hat{S}_1+\hat{S}_9\cdot\hat{S}_{10}\\&+\hat{S}_{10}\cdot\hat{S}_{11}+\hat{S}_{11}\cdot\hat{S}_{12}+\hat{S}_{12}\cdot\hat{S}_{13}+\hat{S}_{13}\cdot\hat{S}_{14}+\hat{S}_{14}\cdot\hat{S}_{15}\\&+\hat{S}_{15}\cdot\hat{S}_{16}+\hat{S}_{16}\cdot\hat{S}_9+\hat{S}_2\cdot\hat{S}_4+\hat{S}_4\cdot\hat{S}_6+\hat{S}_6\cdot\hat{S}_8\\&+\hat{S}_8\cdot\hat{S}_2+\hat{S}_{10}\cdot\hat{S}_{12}+\hat{S}_{12}\cdot\hat{S}_{14}+\hat{S}_{14}\cdot\hat{S}_{16}+\hat{S}_{16}\cdot\hat{S}_{10}\\&+\hat{S}_1\cdot\hat{S}_{17}+\hat{S}_{17}\cdot\hat{S}_9+\hat{S}_3\cdot\hat{S}_{18}+\hat{S}_{18}\cdot\hat{S}_{11}+\hat{S}_5\cdot\hat{S}_{19}\\&+\hat{S}_{19}\cdot\hat{S}_{13}+\hat{S}_7\cdot\hat{S}_{20}+\hat{S}_{20}\cdot\hat{S}_{15}]\end{aligned} \quad (1)$$

The above spin formalism gives rise to spin states with total spin $S_T = 0-10$ with exchange energies listed in Table 2. The degeneracy associated with each S_T state is given by '*n*' in the first column. The solid red line shown in Figure 3 is the fit to the Heisenberg−Dirac−van Vleck equation derived using the energies listed in Table 2.[21] Both the *g* factor and J_{eff} are varied, and the fit parameters are listed in Table 3. The observed small J_{eff} (~−3 K) agrees with our earlier speculation that the ferro- and antiferomagnetic interactions present in Cu_{20} might cancel each other to a high degree and that the latter is the dominant interaction. We note, however, that the fitted parameters are not satisfactory because, for example, the *g* value is found to be less than 2, which is unlikely for Cu^{2+} materials. However, the rather large number of spin states involved in the calculations makes this problem untractable at this point.

Electron Paramagnetic Resonance (EPR) Spectroscopy. To further probe the magnetism of **KLi-1** and **KLi-2**, we employed EPR spectroscopy over the microwave frequency range of 9−220 GHz and temperature range of 5−300 K. Under all the conditions, the measured EPR spectra were typical of traces of Cu^{2+} countercation impurities, with concentrations on the order of 5%. We were unable to identify such minute Cu^{2+} impurities by single-crystal XRD, elemental analysis, or any other technique, which indicates the power of EPR. Figure 4 shows some typical spectra at 34 GHz and 6 K. The spectra exhibit fairly well-resolved hyperfine structures typical of noninteracting Cu^{2+} ions, without any significant feature that could be assigned to the Cu_{20} cluster. This result strongly supports the magnetic susceptibility and magnetization data discussed in the previous section, namely, that the ground state of the Cu_{20} cluster is totally diamagnetic. The observed EPR spectra could be easily analyzed in terms of their **g** tensor and hyperfine tensor components and are collected in Table 3. There are clearly two sites for the Cu^{2+} ions in the molecule, as labeled in the figure. The fact that $g_{||} > g_{\perp}$ and $A_{||} \sim 90$ G suggests that the unpaired electron is in a $d_{x^2-y^2}$ orbital with oxo ligands in a square-planar coordination geometry. We note that the *g* values of these excess spins are much larger than those from susceptibility values of the Cu_{20} cluster. The temperature dependence of **KLi-1** and **KLi-2** at various frequencies shows (data not presented) that the signal intensity from the random Cu^{2+} countercation impurity drops gradually as the temperature is increased, as expected from a Curie−Weiss behavior. No further signals attributable to the Cu_{20} cluster are seen, which was surprising. We surmise that this failure to detect signals is due to the presence of strong spin-exchange effects that cause a severe line broadening.

Table 2. Spin Energy Levels of the $Cu_{20}X$ Cluster Derived from Hamiltonian Given in Eq 1

n	S_T	$E(S_T)$
1	10	$-95J_{eff}$
19	9	$-75J_{eff}$
170	8	$-57J_{eff}$
950	7	$-41J_{eff}$
3705	6	$-27J_{eff}$
10659	5	$-15J_{eff}$
23256	4	$-5J_{eff}$
38760	3	$3J_{eff}$
48450	2	$9J_{eff}$
41990	1	$13J_{eff}$
16796	0	$15J_{eff}$

Electronic Structure. DFT calculations were performed to obtain complementary information on **1**−**3**. The electronic structure and the encapsulation energies of some halides were computed. Structure optimizations have been carried out, and the main geometrical parameters—interatomic distances—are well reproduced using the technique described in the Computational Details section. Despite that magnetic measurements suggest a diamagnetic ground state ($S = 0$) with 20 antiferromagnetically coupled unpaired electrons, we have carried out electronic structure calculations, taking the high-spin solution, namely, with 20 spin-up electrons ($S = 10$). It is worth performing this approximate approach since the electronic structure is qualitatively well-reproduced at a much lower computational cost. Magnetic studies using a fragment approach and a model Hamiltonian are in progress. Preliminary results based on this model show that Cu···Cu metal ions are antiferromagnetically coupled, in agreement with the experiments reported herein. For **1**, the two characteristic and well-defined oxo (occupied) and tungsten (virtual) *bands* have been identified, separated by ca. 1.87 eV at the BP86 level.[22] The particular electronic structure of

(21) (a) Carlin, R. L. *Magnetochemistry*; Springer: Berlin, 1986. (b) Kahn, O. *Molecular Magnetism*; VCH: New York, 1993.

(22) (a) Poblet, J. M.; López, X.; Bo, C. *Chem. Soc. Rev.* **2003**, *32*, 297. (b) López, X.; Maestre, J. M.; Bo, C.; Poblet, J. M. *J. Am. Chem. Soc.* **2001**, *123*, 9571. (c) López, X.; Bo, C.; Sarasa, J. P.; Poblet, J. M. *Inorg. Chem.* **2003**, *42*, 2634. (d) López, X.; Poblet, J. M. *Inorg. Chem.* **2004**, *43*, 6863. (e) Maestre, J. M.; López, X.; Bo, C.; Casañ-Pastor, N.; Poblet, J. M. *J. Am. Chem. Soc.* **2001**, *123*, 3749.

Table 3. Spin-Hamiltonian Parameters of $Cu_{20}X$ Derived from Susceptibility and 34 GHz EPR

	susceptibility		EPR site 1			EPR site 2		
	g	J_{eff}	$g_{\|\|}$	$g_{\perp}$	$A_{\|\|}$ (G)	$g_{\|\|}$	$g_{\perp}$	$A_{\|\|}$ (G)
1	1.71 ± 0.02	-3.04 ± 0.02	2.433 ± 0.005	2.078 ± 0.005	90 ± 10	2.326 ± 0.005	2.078 ± 0.005	160 ± 10
2	1.44 ± 0.02	-3.11 ± 0.02	2.430 ± 0.005	2.080 ± 0.005	90 ± 10	2.334 ± 0.005	2.080 ± 0.005	160 ± 10

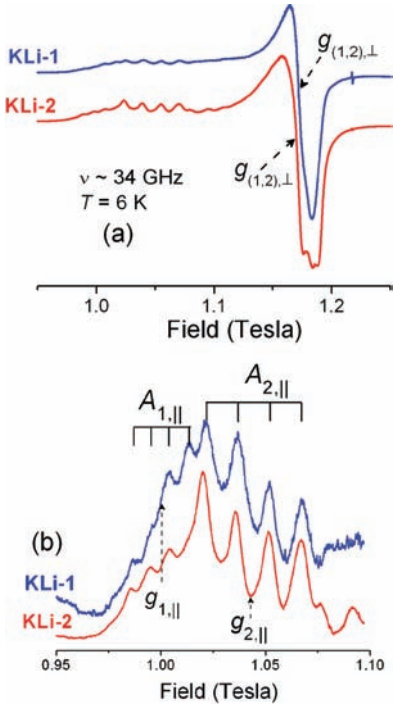

Figure 4. (a) Q-band (~34 GHz) EPR spectra of **KLi-1** and **KLi-2** at 6 K. (b) Magnified view of the $g_{||}$ peaks. The Hamiltonian parameters are summarized in Table 3.

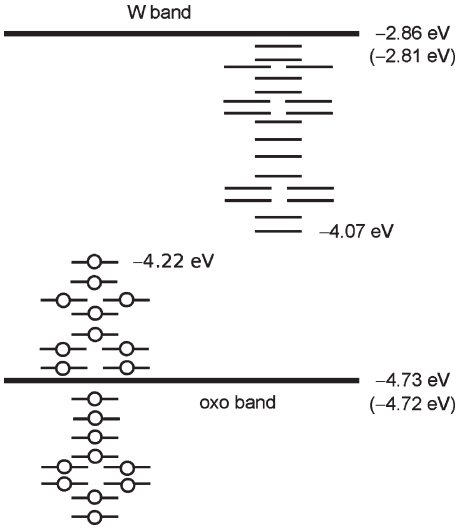

Figure 5. Schematic molecular orbital diagram of the frontier orbital region for **1**−**3**. The α (right) and β (left) sets of orbitals are localized in the Cu−O fragment. Each circle is an electron. The energy values correspond to the solvated polyanion, obtained with a COSMO calculation. In parentheses, we show the orbital energies of the isolated $\{P_8W_{48}\}$ fragment in solution.

this cluster presents 20 singly occupied α orbitals that are found close in energy to the highest oxo orbitals (see Figure 5). Our results suggest that, among the singly occupied Cu-like orbitals, roughly one-half lay below and the other half above the highest occupied oxo orbital. The set of 20 unoccupied β orbitals lays above in energy, between −4.07 and −2.90 eV, the first W-like virtual orbital being found at −2.86 eV. Molecular orbitals containing the unpaired electrons are symmetry-adapted combinations of d(Cu) and p(O) atomic orbitals with some antibonding character (Figure 6). In general, antiferromagnetic systems feature these types of d−p combinations, with electrons coupled through a superexchange mechanism via diamagnetic ligands (oxygen atoms in the present case).

The structural issues for the different systems analyzed (X = Cl, Br, I) show that the Cu_{20} framework remains unaltered along this series of halogens, revealing that the interactions are weak to the point that these are almost independent of the size of X. A similar conclusion arises observing the atomic net charges. Assuming a high-spin state ($S = 10$), with all copper centers with a d^9 configuration, the multipole-derived charges vary little from one X to another (Table 4).[23] For the chloride derivative, the two types of Cu centers carry charges of +0.645 and +0.781, which turn to +0.646 and +0.777 for X = Br and +0.602 and +0.775 for X = I.

One can envisage the possibility of anionic exchange in polyanions **1**−**3**. The cavity in the center of the Cu_{20} fragment can encapsulate a relatively small anion such as a halide that potentially could be released from the cavity. The escape of the halide anions X^-, with X = Cl, Br, and I, has been analyzed at the DFT level. Figure 7 shows the energy profile computed for the set of X^- by means of a scan of geometries ($\{P_8W_{48}\}$ ring frozen and Cu_{20} fragment reoptimized at each step). We can observe that the energy profile for **1** exhibits a minimum in the center of the cavity in excellent agreement with the X-ray structure, which shows that Cl^- is located in the center of the cavity. It is also interesting to observe that, when the Cl^- ion moves along the C_4 symmetry axis, the energy increases, but very smoothly at the beginning, suggesting that the Cl^- may occupy a wide region inside the cavity. When the displacement is larger than 1 Å, the energy increases with a greater slope reaching a barrier of 90 kcal mol^{-1} when the halide crosses the window constituted by the Cu_4O_4 ring. The barriers increase with the size of the anion, being ca. 100 kcal mol^{-1} for $X = Br^-$ and 120 kcal mol^{-1} for $X = I^-$. The results show that the energy requirements for anion release are far from being achievable even at high temperatures. The behavior observed for **1**−**3** contrasts with the cation exchange in the Preyssler ion $[X^{n+}P_5W_{30}O_{110}]^{(15-n)-}$, where it is well established that

(23) Swart, M.; van Duijnen, P. T.; Snijders, J. G. *J. Comput. Chem.* **2001**, *22*, 79.

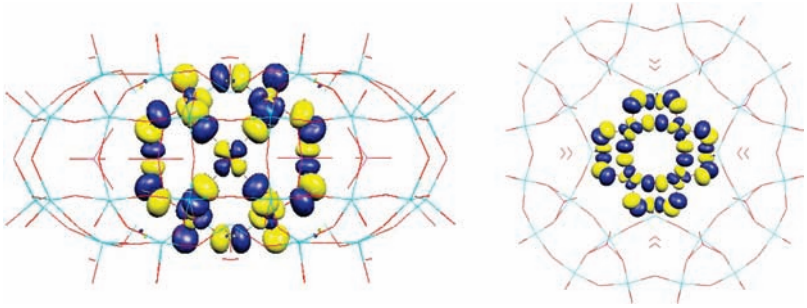

Figure 6. Side and top 3D representations of a singly occupied molecular orbital, localized in the Cu_{20} moiety.

Table 4. Selected Multipole-Derived (MDC-q) Atomic Net Charges and Spin Densities for the Compounds Analyzed at the DFT Level

	Cl^-	Br^-	I^-
	Net Charges		
X	−0.628	−0.595	−0.172
Cu(1)	+0.643	+0.648	+0.598
Cu(2)	+0.781	+0.777	+0.775
Cu(3)	+0.648	+0.644	+0.606
	Spin Density		
X	0.071	0.0071	0.071
Cu(1)	0.414	0.414	0.414
Cu(2)	0.423	0.422	0.422
Cu(3)	0.428	0.428	0.428

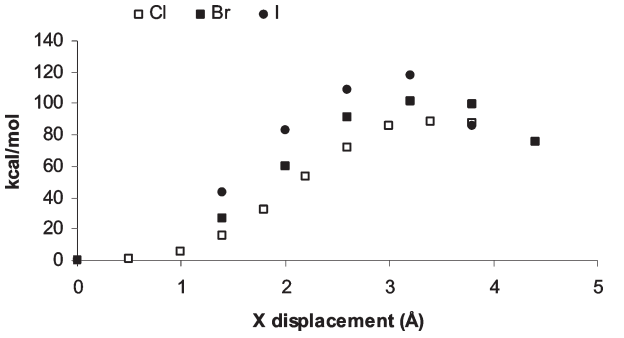

Figure 7. Scan of geometries for the displacement of X = Cl, Br, and I along the C_4 axis. The first point is the geometrical center of the cluster; the last one corresponds to the anion out of the cavity.

the encapsulated cation can be released from the internal cavity. Using a similar procedure, the energy barrier for this process was found to range from 40 kcal mol^{-1} for Na^+ to 70 kcal mol^{-1} for Th^{4+}.[24] The difference in the behavior of anion and cation exchange in the $\{Cu_{20}P_8W_{48}\}$ and Preyssler-type polyanions, respectively, very probably originates from the larger radii of the halides with respect to the cations.

Electrochemistry. Before studying the redox properties of **2** and **3**, it was necessary to determine their stability domains over the pH scale being used (detailed data are included in the Supporting Information). Figure 8A shows the cyclic voltammogram (CV) of **2** in a pH 5 medium. The reduction pattern is composed of four reduction waves located respectively at −0.162, −0.211, −0.688, and −0.806 V versus SCE. On an expanded

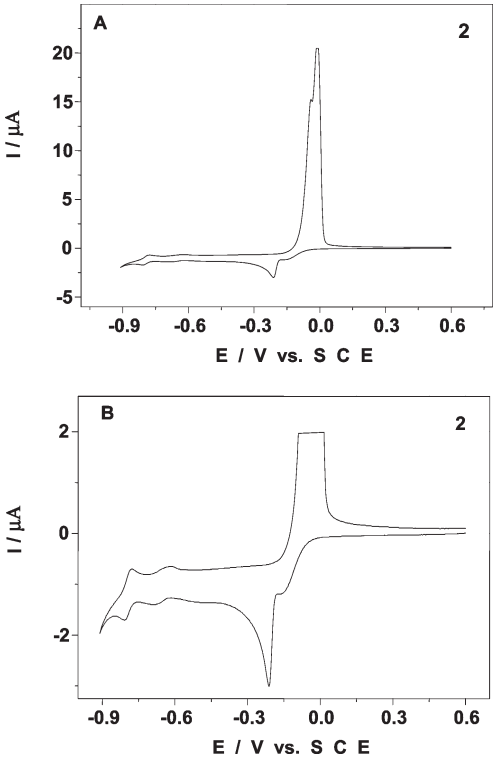

Figure 8. (A) Cyclic voltammogram of a 4×10^{-5} M solution of **2** in a 1 M CH_3COOLi + CH_3COOH (pH 5) medium. The scan rate was 2 mV s^{-1}. The working electrode was glassy carbon (3 mm diameter disk), and the reference electrode was SCE. (B) Magnification of A to highlight the W^{6+} reduction waves. The copper reoxidation wave was truncated.

current scale, Figure 8B highlights the last two waves which are chemically reversible and feature the reduction of W^{6+} centers. Their CV characteristics are close to those of the precursor $\{P_8W_{48}\}$ (Figure S3, Supporting Information). At this pH, each of the two tungsten waves corresponds to the consumption of eight electrons per molecule.[25] The first two waves are attributed to the reduction in two steps of Cu^{2+} to Cu^0 through Cu^+. This behavior is in line with the observations made with **1**[5a] and other Cu^{2+}-substituted POMs[26] under the same experimental conditions. On the scan going towards positive voltage, the large desorptive oxidation wave

(24) Fernández, J. A.; López, X.; Bo, C.; de Graaf, C.; Baerends, E. J.; Poblet, J. M. *J. Am. Chem. Soc.* **2007**, *129*, 12244.

(25) Keita, B.; Lu, Y. W.; Nadjo, L.; Contant, R. *Electrochem. Commun.* **2000**, *2*, 720.

(26) (a) Keita, B.; Mbomekalle, I.-M.; Nadjo, L.; Contant, R. *Electrochem. Commun.* **2000**, *2*, 720. (b) Nellutla, S.; van Tol, J.; Dalal, N. S.; Bi, L.-H.; Kortz, U.; Keita, B.; Nadjo, L.; Khitrov, G. A.; Marshall, A. G. *Inorg. Chem.* **2005**, *44*, 9795. (c) Pichon, C.; Mialane, P.; Dolbecq, A.; Marrot, J.; Rivière, E.; Keita, B.; Nadjo, L.; Sécheresse, F. *Inorg. Chem.* **2007**, *46*, 5292.

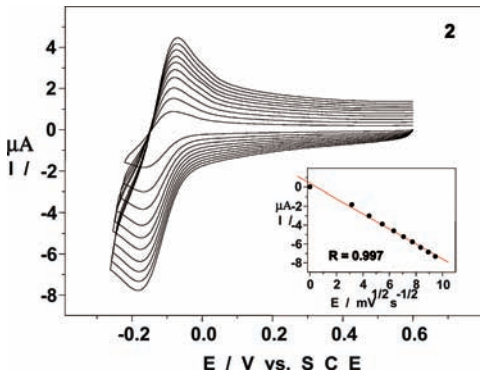

Figure 9. Cyclic voltammograms of 4×10^{-5} M solution of **2** in a 1 M $CH_3COOLi + CH_3COOH$ (pH 5) medium. The scan rates (from inner to outer curve) are 10, 20, 30, 40, 50, 60, 70, 80, 90, and 100 mV s^{-1}. The working electrode was glassy carbon (3-mm-diameter disk), and the reference electrode was SCE. The potential reversal is fixed after the Cu^{2+} to Cu^{+} redox process. (Inset) Variations of the cathodic peak current intensities as a function of the square root of the scan rate.

observed at −0.015 V versus SCE is characteristic of surface-confined species and features an overlap of the oxidation of the deposited Cu^0 with the reoxidation wave of Cu^+ centers. These oxidation waves are only separated by roughly −0.065 V. Figure 9 presents the variations of the CV of **2**, restricted to the Cu^{2+} to Cu^+ process, as a function of the potential scan rate, and it can be seen that well-defined CVs are obtained. The variation of the cathodic peak current intensity as a function of the square root of the scan rate is also shown in Figure 9. The good linearity of this curve indicates that the Cu^{2+}/Cu^+ electron transfer is mainly controlled by a diffusion process. The results altogether converge to explain why the Cu^+/Cu^{2+} diffusion wave is much smaller than the oxidation current of Cu^0, which features a surface-controlled process. Furthermore, comparison of the peak current intensities for the Cu^{2+} to Cu^+ reduction processes of **1**, **2**, and **3** to that of the first eight-electron W-wave of the $\{P_8W_{48}\}$ tungstophosphate wheel indicates that 20 electrons are involved in the first reduction step of the Cu^{2+} centers (with the assumption that the diffusion coefficients of $\{P_8W_{48}\}$ and polyanions **1**, **2**, and **3** are similar). In other words, all 20 Cu^{2+} ions of the polyanions are involved in this first step. These observations demonstrate a stabilization of Cu^+ by the $\{P_8W_{48}\}$ ligand, at least during the time scale of the CV runs. Structural changes could occur upon reduction, but a detailed study of these processes is beyond the scope of this paper. No significant amount of free Cu^{2+} countercation impurities could be detected by cyclic voltammetry.

The shape of the CV of **3** resembles the one observed for **2** the same experimental conditions. Table S5 (Supporting Information) gathers the main voltammetric characteristics for the CVs of **2** and **3** in a pH 5 medium. For comparison, the corresponding data obtained with **1** are included. The potential locations of the Cu or W waves of the three analogues do not depend significantly upon the identity of the halogen X. A comparison of the peak current intensities for the Cu^{2+} to Cu^+ reduction processes for **2** and **3** and $CuSO_4$ indicates that the diffusion coefficients of **2** and **3** are roughly 6.3 times smaller than that of $CuSO_4$, thus demonstrating that the Cu^{2+} ions remain within the polyanion in solution. This result confirms the observed stability of **2** and **3** by UV−visible spectroscopy performed at pH 5.

For **2** and **3**, a fifth reduction wave with a large current intensity was observed, associated with the deposition of Cu^0 (not shown), when the potential was swept negatively to the potential domain where the last reversible W wave appears. This large irreversible wave features the hydrogen evolution reaction, in line with previous observations in the case of **1**[5a] and other Cu-substituted POMs.[26c,27]

Exhaustive electrolyses of **2** and **3** were carried out at pH = 5 (at −0. 550 V versus SCE). For both compounds, the number of electrons consumed per Cu is 2.0 ± 0.1, thus indicating that all of the copper centers are two-electron-reduced. When the fixed potential is more negative than −0.6 V versus SCE, the reduction of the W centers triggers an electrocatalysis of solvent reduction far stronger than the one observed with the precursor $\{P_8W_{48}\}$.

Some characteristics of the previous[5a] and present electrochemical data can be analyzed from the electronic structure of polyanions **1**−**3**. The first orbital ready to accept an extra electron in **1** is found at −4.07 eV, localized in the Cu_{20} fragment. Besides the other empty Cu-like orbitals that are found at slightly higher energies, the first W-like empty orbital appears at −2.86 eV. The rather large energy gap between these two Cu- and W-like empty orbitals agrees with the large separation observed in the reduction waves of Cu and W. The orbital energies of the frontier orbitals are independent of the central halide; as a matter of fact, the reduction bands in the CVs remain hardly unaltered in the three studied anions **1**−**3**.

The isolated $[P_8W_{48}O_{184}]^{40-}$ fragment was also computed with the solvent. It features orbital energies of −4.72 and −2.81 eV for the highest oxo and lowest tungsten orbitals, respectively. These are roughly the same as the DFT values obtained for **1** (−4.73 and −2.86 eV, respectively). The energy gap between both bands consequently remains the same, ∼1.9 eV. This result matches the CVs at pH = 5, where the first reduction wave of $\{P_8W_{48}\}$ (W wave) appears at roughly the same potential as the W wave in **1**. This suggests that the Cu_{20} moiety just replaces the countercations inside the cavity created by the $\{P_8W_{48}\}$ fragment without modifying its electronic structure. For comparison, when the same method of calculation is applied to the $[NaP_5W_{30}O_{110}]^{14-}$ Preyssler anion, a large POM cluster with similar characteristics, we find a LUMO at −4.0 eV in solution, much more stable than that of $[P_8W_{48}O_{184}]^{40-}$. This fact can be understood considering the total charge of each system and taking into account the number of metal atoms supporting this charge.[28] Since the number of W atoms largely surpasses the charge in the Preyssler anion, the LUMO is very stable. On the other hand, as 48 tungstens is roughly the same as the number of negative charge units (40) in $\{P_8W_{48}\}$, the molecular orbitals are strongly destabilized. The reader must be aware that the final energy of the LUMO and

(27) (a) Keita, B.; Nadjo, L. Electrochemistry of Isopoly and Heteropoly Oxometalates. *Encyclopedia of Electrochemistry*; Bard, A. J., Stratmann M., Eds.; Wiley-VCH: New York, 2006; Vol. 7, p 607. (b) Keita, B.; Nadjo, L. *J. Mol. Catal. A: Chem.* **2007**, *262*, 190.

(28) López, X.; Fernández, J. A.; Poblet, J. M. *Dalton Trans.* **2006**, 1162.

therefore the redox properties of the anion also depend on the degree of protonation, which is related to the pH of the solution.

Modified Electrodes Based on 2 and Room-Temperature Ionic Liquid (1-Butyl-3-methylimidazolium Tetrafluoroborate): Electrocatalysis of Nitrate Reduction. Electrocatalysis of the transformation of nitrate to environmentally harmless compounds or even energetically valuable chemicals remains a challenge because these processes require several electrons. Among the scarce examples of POM-based electrocatalysts for nitrate reduction, the multicopper substituted POMs are the most efficient.[5a,29b,30] The polyanion **2** was selected to investigate the electrocatalytic abilities of modified electrodes based on **2** and **BMImBF$_4$**. Room-temperature ionic liquids (RTILs) are widely used electrolytes for the fabrication of modified electrode materials with various compounds, as proposed in the pioneering work of Wadhawan et al.[31a] The advantages of using RTILs for the preparation of POM-modified electrodes have also been reported.[31b] Huang et al. showed that glassy carbon modified electrodes based on $H_3PMo_{12}O_{40}$ and **BMImBF$_4$** exhibit good electroactivity.[19] They also demonstrated that the successful immobilization of $[PMo_{12}O_{40}]^{3-}$ anions is mainly due to electrostatic interaction with **BMIm**$^+$ cations adsorbed on the glassy carbon electrode. However, to our knowledge, there is no report of electrocatalytic nitrate reduction by a POM entrapped in a RTIL.

We tested the electroactivity of **2** dissolved in the pH 5 medium for the reduction of nitrate, prior to the investigations of **2**-based modified electrodes for this reaction. Figure S4 (Supporting Information) shows the CVs recorded in the absence and presence of nitrate. The electrocatalytic process onsets at the potential location of the first W wave. Upon increasing the nitrate concentration, the catalytic current rises, even for modest values of the excess parameter γ (γ is defined here as $\gamma = C^0$ (nitrate)/C^0 (**2**)). As expected, we find out that, under the same experimental conditions, **2** and its analogue **1**[5a] exhibit comparable activities toward nitrate reduction, according to their similar redox properties, as described above. Furthermore, **2** reduces nitrate beyond the state of nitrite because the reduction of nitrite by **2** is far easier than that of nitrate (Figure S4, Supporting Information). Therefore, the product of the electrocatalytic process is N_2O, but perhaps also more reduced compounds. It is likely that **2** reduces nitrate beyond the state of N_2O because a large number of electrons is involved in the potential domain where this reduction takes place. Large-scale bulk electrolyses coupled with other techniques such as chromatography are necessary to determine the product(s) of the electrocatalytic process, including quantitative aspects. The superior efficiency of these POMs, compared with other Cu-substituted POMs, is attributed[5a] to both the accumulation of Cu centers and also to the possibility to fabricate highly reduced species with the electrons accumulated in the reduced W framework of the POM.

The **2**-modified electrodes were prepared with a **BMImBF$_4$** solution of **2** (**2@BMImBF$_4$**). Their CVs, recorded at pH 5, show that both the Cu and W centers remain electroactive. Figure S5 (Supporting Information) shows the variations of the CV, restricted to the Cu^{2+} to Cu^+ process, for several potential scan rates. The inset plot in Figure S5 presents the linear dependence of the reduction peak current intensity on scan rate, thus indicating a surface-controlled electrochemical process. A perfect reproducibility of the CVs during prolonged potential cycling attests that the electrodes are durable. The operational parameters study of modified electrodes fabrication (concentration of POM, film thickness, etc.) will be carried out with various RTILs.

Figure S6 (Supporting Information) illustrates the ability of the **2@BMImBF$_4$**-modified electrode to electrocatalyze the reduction of nitrate. In the explored potential domain, glassy carbon or ITO modified only with **BMImBF$_4$** does not show any electrocatlytic activity for nitrate reduction. As expected,[5a] the catalytic process onsets at the potential location of the first W-wave. The inset shows a linear peak current increase with the concentration of nitrate. Note that the modified electrodes are very efficient because such good linearity was obtained, even for small concentrations of nitrate in the range 9.0×10^{-6} M to 100×10^{-6} M. The nitrate reduction appeared to be diffusion-controlled. These observations open the way for detection, quantification, and transformation of this chemical by multi-Cu^{2+}-substituted POMs.

Conclusions

We have successfully synthesized and structurally characterized the Cu_{20}-containing tungstophosphates $[Cu_{20}Br(OH)_{24}(H_2O)_{12}(P_8W_{48}O_{184})]^{25-}$ (**2**) and $[Cu_{20}I(OH)_{24}(H_2O)_{12}(P_8W_{48}O_{184})]^{25-}$ (**3**), which represent the bromide and iodide analogues of $[Cu_{20}Cl(OH)_{24}(H_2O)_{12}(P_8W_{48}O_{184})]^{25-}$ (**1**). Magnetic susceptibility and magnetization data over 1.8−300 K show that the Cu^{2+} ions in **1** and **2** are antiferromagnetically coupled, leading to a diamagnetic ground state. DFT calculations indicate that the central halides have some flexibility within the central cavity but cannot be released, even at high temperatures, without destruction of the POM framework. The electrochemical characteristics of **1**−**3** are very similar, in agreement with conclusions of DFT calculations. The comparison of peak current intensities for Cu^{2+} to Cu^+ reduction processes for **2**, **3**, and $CuSO_4$ demonstrates that the Cu^{2+} cations remain bound in the polyanion in solution, which is in agreement with UV−visible spectroscopy performed at pH 5. The polyanion **2** was successfully entrapped within RTIL films. Furthermore, the films were found to be stable and efficient in the reduction of nitrate. We have also prepared several other transition-metal-containing (e.g., Co^{2+}, Mn^{2+}, Ni^{2+}, V^{5+}) derivatives of $\{P_8W_{48}\}$, which will be reported elsewhere.

Acknowledgment. U.K. acknowledges support from Jacobs University, the German Science Foundation

(29) (a) Keita, B.; Nadjo, L. Electrochemistry of Isopoly and Heteropoly Oxometalates Encyclopedia of Electrochemistry; Bard, A. J., Stratmann, M., Eds.; Wiley-VCH: New York, 2006; Vol. 7, p 607. (b) Keita, B.; Nadjo, L. *J. Mol. Catal. A: Chem.* **2007**, *262*, 190.

(30) Zhang, Z.; Qi, Y.; Qin, C.; Li, Y.; Wang, E.; Wang, X.; Su, Z.; Xu, L. *Inorg. Chem.* **2007**, *46*, 8162.

(31) (a) Wadhawan, J. D.; Schröder, U.; Neudeck, A.; Wilkins, S. J.; Compton, R. G.; Marken, F.; Consorti, C. S.; De Souza, R. F.; Dupont, J. *J. Electroanal. Chem.* **2000**, *493*, 75. (b) Liu, H.; He, P.; Li, Z.; Sun, C.; Shi, L.; Liu, Y.; Zhu, G.; Li, J. *Electrochem. Commun.* **2005**, *7*, 1357.

(DFG KO-2288/3-2), and the Fonds der Chemischen Industrie. We thank Abhishek Banerjee for performing the NMR experiments and Dr. M. H. Dickman for help with XRD. N.S.D. and J.v.T. would like to acknowledge the State of Florida and NSF Cooperative Agreement grants DMR-0654118 and DMR-0520481 for financial support. This work was also supported by the CNRS and the University Paris−Sud 11 (UMR 8000). The help of Mrs. Wided Bellagha Chenchah during the preliminary experiments of this work is thankfully acknowledged. J.M.P. thanks the Spanish MICINN (CTQ2008-06549-C02-01/BQU) and the DURSI of the Generalitat de Catalunya (2009SGR462). X.L. thanks the Ramón y Cajal program. Figure 1 was generated by Diamond, version 3.2c (copyright Crystal Impact GbR).

Supporting Information Available: Additional figures and tables and a crystallographic information file. This material is available free of charge via the Internet at http://pubs.acs.org.